

Individual pulse emission from the diffuse drifter PSR J1401–6357 using the ultrawideband receiver on the Parkes radio telescope

J. L. Chen,¹ Z. G. Wen,^{2,3,4,5*} X. F. Duan,^{2,4} D. L. He,² N. Wang,^{2,3} H. G. Wang,^{6,2} R. Yuen,²

J. P. Yuan,^{2,3} W. M. Yan,^{2,3} Z. Wang,^{7,2} C. B. Lv,⁶ H. Wang,¹ S. R. Cui,¹

¹Department of Physics and Electronic Engineering, Yuncheng University, Yuncheng, Shanxi, 044000, People's Republic of China

²Xinjiang Astronomical Observatory, Chinese Academy of Sciences, 150, Science-1 Street, Urumqi, Xinjiang, 830011, People's Republic of China

³Key laboratory of Radio Astronomy, Chinese Academy of Sciences, Nanjing, 210008, People's Republic of China

⁴Key Laboratory of Microwave Technology, Urumqi, Xinjiang, 830011, People's Republic of China

⁵Guizhou Provincial Key Laboratory of Radio Astronomy and Data Processing, Guiyang, Guizhou, 550001, People's Republic of China

⁶School of Physics and Electronic Engineering, Guangzhou University, 510006, Guangzhou, People's Republic of China

⁷School of Physical Science and Technology, Xinjiang University, urumqi, Xinjiang, 830046, People's Republic of China

Accepted 2022 December 03. Received 2022 November 21; in original form 2022 August 13

ABSTRACT

In this study, we report on a detailed single pulse analysis of the radio emission from the pulsar J1401–6357 (B1358–63) based on data observed with the ultrawideband low-frequency receiver on the Parkes radio telescope. In addition to a weak leading component, the integrated pulse profile features a single-humped structure with a slight asymmetry. The frequency evolution of the pulse profile is studied. Well-defined nulls, with an estimated nulling fraction greater than 2%, are present across the whole frequency band. No emission is detected with significance above 3σ in the average pulse profile integrated over all null pulses. Using fluctuation spectral analysis, we reveal the existence of temporal-dependent subpulse drifting in this pulsar for the first time. A clear double-peaked feature is present at exactly the alias border across the whole frequency band, which suggests that the apparent drift sense changes during the observation. Our observations provide further confirmation that the phenomena of pulse nulling and subpulse drifting are independent of observing frequency, which suggest that they invoke changes on the global magnetospheric scale.

Key words: stars: neutron – pulsars: – general – pulsars: individual (J1401–6357)

1 INTRODUCTION

Pulsars are famous as precise clocks in the areas of fundamental physics under extreme conditions (Deng et al. 2020, 2021; Gao et al. 2021; Yan et al. 2021), which are attributed to the exceptionally regular rotation and stable integrated pulse profiles. The integrated pulse profiles derived from averaging over tens of thousands of pulses are highly stable for the majority of pulsars, and remain stable temporally. In contrast, a myriad of intrinsic amplitude and phase modulation effects are displayed in the sequential rotations of a pulsar, which directly reflects the variation in the magnetosphere. Occasionally, the pulse emission quenches abruptly for a period of time, which has been dubbed as nulling (Backer 1970b), and the phenomenon has been detected in more than 200 pulsars. Pulse nulling appears to occur at all frequencies and to all components simultaneously, but partial nulls are also detected (Wang et al. 2007). A variety of models have been proposed for nulling, such as orbital companions (Cordes & Shannon 2008), missing line of sight (Herfindal & Rankin 2007), switching between curvature radiation and inverse Compton scattering (Zhang et al. 1997), non-radial oscillations (Rosen et al. 2011), precessional torques (Jones 2012), magnetic field instability (Geppert et al.

2003), switching between magnetospheric states (Timokhin 2010), and the modification of surface magnetic field (Geppert et al. 2021). Amongst the most promising theories is the possibility that the pulsar magnetosphere experiences systematic variation in the global charge distribution (Lyne et al. 2010). In some pulsars, the subpulses were observed to perform systematic drift motion within the pulse window, which is termed as subpulse drifting phenomenon (Drake & Craft 1968). The periodic phase-modulated drifting appears to be a universal behaviour, and has been reported in at least one-third of the normal pulsars (Weltevrede et al. 2006) and in some millisecond pulsars (Edwards & Stappers 2003). The sparking model for subpulse drifting as suggested by Ruderman & Sutherland (1975) has been widely accepted, in which a number of sparks discharge in a gap over the polar cap and circulate around the magnetic pole in the pulsar magnetosphere. Recently, several studies have highlighted the limitations for the interpretations of sparking discharges. van Leeuwen & Timokhin (2012) suggested that changes in the drift velocity are dependent on the variation in the accelerating potential across the polar cap, and employed multipoles to model the subpulse drift reversals. Wright & Weltevrede (2017) explained the phenomenon of bi-drifting subpulses by suggesting that the carousel beams are elliptical with axes tilted relative to the fiducial plane. Szary & van Leeuwen (2017) introduced the effect of non-dipolar

* E-mail: wenzhigang@xao.ac.cn

magnetic fields, and proposed that the plasma in the inner acceleration region rotates around the point of maximum potential at the polar cap. [Basu et al. \(2020a, 2022\)](#) suggested that the variable drift of the sparks in the partially screened gap lags behind the corotation motion of the pulsar. [Wright \(2022\)](#) proposed that the emission patterns are originated from an internal system with beat frequency between the magnetospheric drift and the delay time in the rotation of the magnetosphere. The pulse nulling and subpulse drifting phenomena are important in shaping ideas concerning the pulsar radio emission process.

PSR J1401–6357 is a normal pulsar with rotational period of $P_1 = 0.84$ s. It has a narrow pulse profile with a duty cycle of 4.72% ([Hobbs et al. 2004](#)). The linear polarization has been shown to be moderate with a gentle variation in position angle ([Qiao et al. 1995](#)). On the contrary, the more sensitive polarization behaviour reported by [Johnston & Kerr \(2018\)](#) shows large variations in the polarization position angle, indicating a core single profile. Infrequent short nulls are observed, which give a nulling fraction (NF) of just 1.6% at 1369 MHz ([Wang et al. 2007](#)).

In this paper, we focus on the properties of the individual pulse emission from PSR J1401–6357 across ultrawide frequency band. In Section 2, we describe the observations, which used the ultrawide bandwidth low-frequency (UWL) receiver on the Parkes radio telescope, the data reduction, and the data analysis. Investigation of the average pulse profiles, pulse nulling and the subpulse drifting is presented in Section 3. Discussion and conclusions are given in Sections 4 and 5, respectively.

2 OBSERVATIONS AND DATA PROCESSING

The analyses in this paper are based on available observations from the Parkes pulsar data archive¹ ([Hobbs et al. 2011](#)), which were carried out using the UWL receiver on the Parkes 64 m radio telescope on 26 November 2018. The frequency-dependent system-equivalent flux density ranges from 33 to 72 Jy ([Hobbs et al. 2020](#)). The UWL radio frequency band (704–4032 MHz) is subdivided into 3328×1 MHz frequency channels. The four polarization-product data are processed by the ‘Medusa’ graphics processing unit cluster and written to disc in PSRFITS² search-mode format ([Hotan et al. 2004](#)) with 8-bit quantization. The pulsar was successively observed with time resolution of 64 μ s for around 1 hour.

In the off-line data processing, the raw filterbank data were initially processed to mitigate spurious radio frequency interference (RFI) signals. The frequency channels at subband boundaries were zero-weighted. The RFI-affected frequency channels were identified and flagged using a median-filter technique. Subsequently, the data from each channel were incoherently dedispersed at the dispersion measure of the pulsar ($DM=98.0$ pc cm⁻³) to correct for the frequency-dependent spread caused by the dispersive effects of the interstellar plasma. After that, the data were averaged into eight separated subbands, each having an equal bandwidth of 416 MHz, to study the frequency evolution of the pulsar emission. Finally, using the pulsar ephemerides from the ATNF pulsar catalogue³ ([Manchester et al. 2005](#)), the data were re-sampled and folded at the topocentric spin period to extract a three-dimensional pulse-stack with 1024 longitude bins on the x-axis, 4210 pulses on the y-axis, and 8 frequency subbands on the z-axis.

¹ <https://data.csiro.au>

² <http://www.atnf.csiro.au/research/pulsar/psrfits/>

³ <http://www.atnf.csiro.au/people/pulsar/psrcat/>

As an example of the output of the data processing, the single pulse sequences and their corresponding average pulse profiles at eight different frequencies across the band of the UWL are shown in Figure 1. Prominent burst pulses are interspersed with nulls at all frequencies concurrently.

3 RESULTS

3.1 Average pulse profile

The behaviour of a radio pulse profile as frequency evolves sheds insight into the emission geometry of the pulsar, including the height of the emission region, the beam shape, radius-to-frequency mapping (RFM) and so on. The pulsar radiation models can be further constrained by studying the morphologies of pulse profiles in multi-bands. PSR J1401–6357 was reported to have a narrow pulse profile with a weak extension in the leading side ([Hobbs et al. 2004](#)). The prominent component is composed of a conflated core and trailing conal outrider at 1.4 GHz ([Johnston & Kerr 2018](#)). PSR J1401–6357 has been regarded as having a core-single (S_r) profile ([Rankin 2022](#)), according to the morphological classification for pulse profiles proposed by [Rankin \(1983\)](#). The average pulse profiles of PSR J1401–6357 at eight observing frequencies are displayed in Figure 2, where the pulse peaks are normalized to unity. It is remarkable that the pulse profile changes with frequency in a characteristic manner. As the frequency decreases, the core component becomes more and more asymmetric in shape. In general, the core components have widely asymmetric shapes and bifurcations. Such effects were also observed in PSR B1933+16, which is a core-emission-dominated pulsar, and exhibits a very clear non-Gaussian structure with notches ([Mitra et al. 2016](#)). At high frequencies, its two outriders become more and more intensive when comparing with the main component ([Sieber et al. 1975](#)). The core emission from the mode changing pulsar B0329+54 is found to be intensity-dependent. The stronger core emission that appears at the leading part of the component is interpreted as due to the aberration/retardation effect ([Brinkman et al. 2019](#)). The asymmetrical structures shown in the profile components are proposed to originate from intrinsic effects, such as the plasma generation process and emission mechanism, as well as propagation effects in the pulsar magnetosphere. As a result the Gaussian fitting analysis described by [Kramer \(1994\)](#) often leads to improper identification of the individual components, which is not applicable in the present case.

The weak leading component is located in pulse longitude ranging from 170° to 176°. By studying the individual pulse emission at 1369 MHz, [Wang et al. \(2007\)](#) argued that the weak leading component was formed from highly sporadic pulses. In addition, the occasional pulses are comparable in flux density to those at the main peak. The modulation index is a measure of the factor by which the intensity varies from pulse to pulse ([Weltevrede et al. 2006](#)). Therefore, it is taken as an indication for the presence of subpulses. To identify the sporadic leading outbursts, the longitude-resolved modulation index is calculated, which is defined as $m_i = \sigma_i / \mu_i$, where σ_i is the standard deviation and μ_i is the mean intensity in the i -th bin. In Figure 3, the black line is the longitude-resolved standard deviation and the red line corresponds to the longitude-resolved modulation index. The longitude-resolved modulation index varies a lot with pulse longitude. It shows a minimum in the middle of the pulse profile where the total intensity is relative high. A sharp peak at the leading edge of the pulse profile is presented in the longitude-resolved modulation index, which is caused by bright subpulses. To

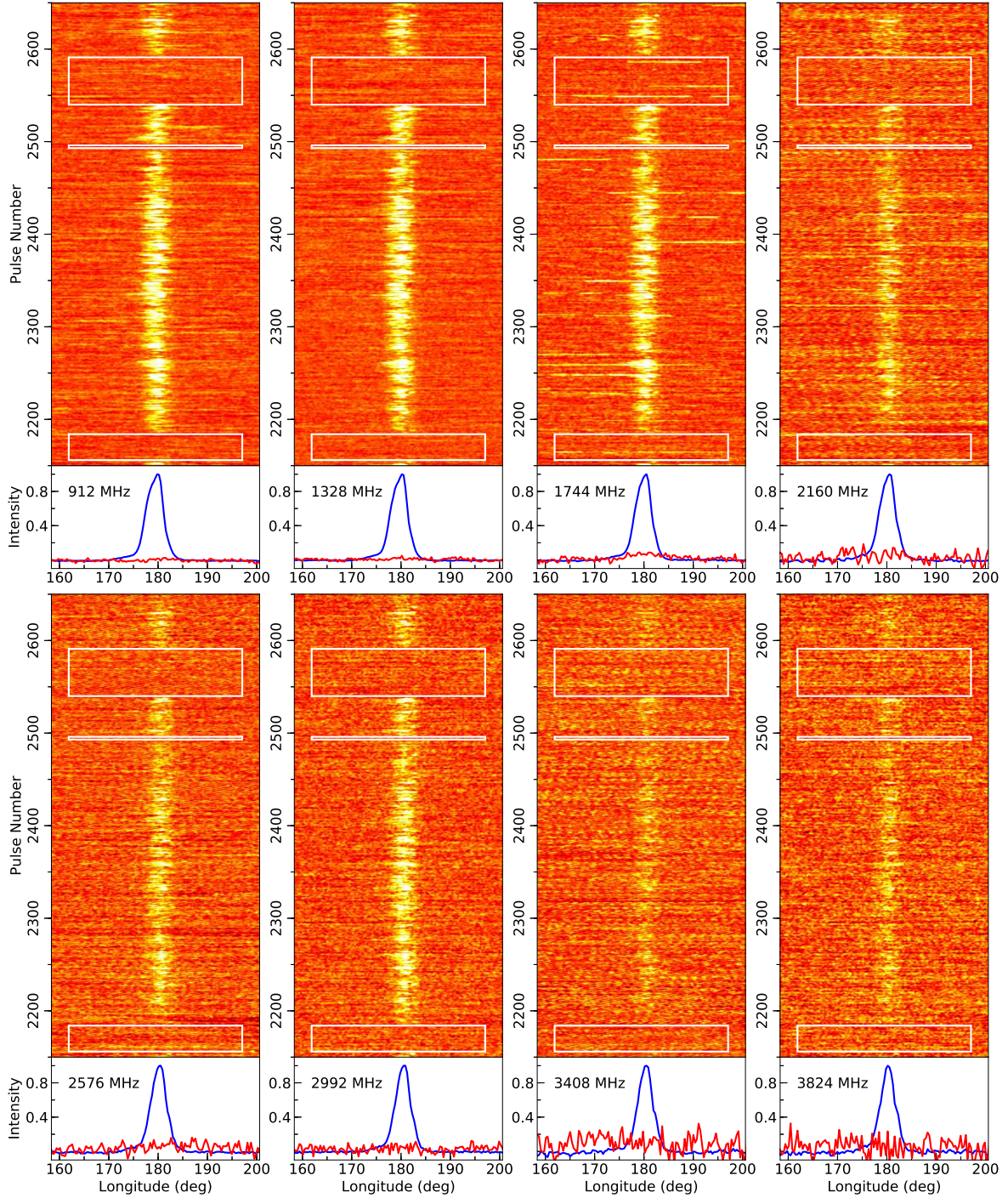


Figure 1. Plots showing the single pulse stacks for PSR J1401–6357 at eight different frequencies across the UWL band, with their corresponding average pulse profiles (blue) shown in the bottom panels. The three intervals of quenching emission are indicated by the white rectangles in each plot. The averaged null pulse profiles are shown with red lines. No significant emission is present in the null pulse profiles. The average profiles are normalized by the peak amplitude of the burst profiles.

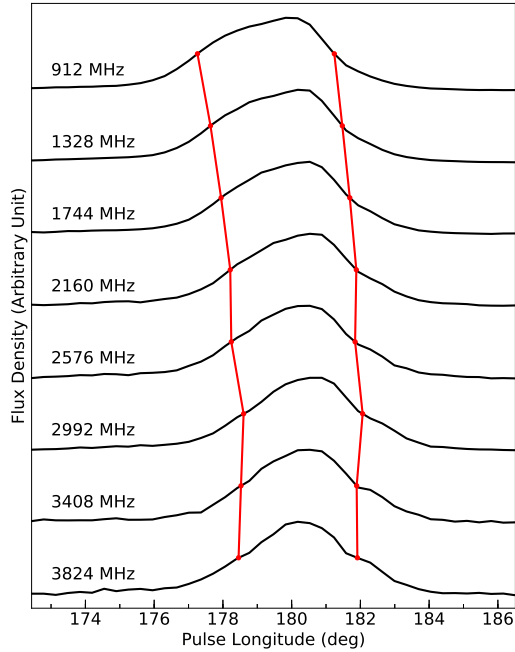


Figure 2. Broadband pulse profiles of PSR J1401–6357. The black solid lines represent the observed profiles. The red dots indicate the W_{50} of the pulse profiles.

separate pulses with the presence of sporadic leading bursts, the relative pulse energies are calculated for the leading edge of the profile. The occurrence of the sporadic emission in the leading part of the profile is rather rare, with only 184 pulses out of 4210 pulses having pulse energies six times greater than the average. Figure 4 presents the relative pulse energy distribution for the leading edge of the profile. To obtain a more accurate estimate, only the pulses where the bursts were present are included in the distribution. The best power-law fit to the pulse energy distribution gives an index of -6.3 ± 0.3 . Figure 5 shows the average pulse profiles in the presence and absence of the sporadic leading part. It is obvious from the figure that the profiles are different. For the integrated pulse profile with the presence of the sporadic leading part, the relative intensity at the leading edge of the profile is larger and the pulse width is significantly broader. In addition, the central component is stronger during the burst state compared to the normal state.

The mean pulse profile width at 50% (W_{50}) of the peak amplitude is calculated for the eight frequency bands. Considering just one component above the 50% level is shown in the mean pulse profiles, the uncertainty in W_{50} is estimated to be

$$\sigma_{W_{50}} = \frac{W_{50}}{\sqrt{2} \ln(2) S/N}, \quad (1)$$

where S/N is the signal-to-noise ratio of the profile. Figure 6 shows the frequency evolution of the profile width. It is apparent from the figure that the value of W_{50} decreases with increasing frequency, which roughly agrees with a power-law function. The power-law index is estimated to be -0.11 ± 0.01 . In Figure 2, the W_{50} for each frequency is also plotted. The frequency evolution of the profile width during the leading burst state is shown in Figure 7. The pulse width at 10 per cent (W_{10}) level of the peak intensity is calculated

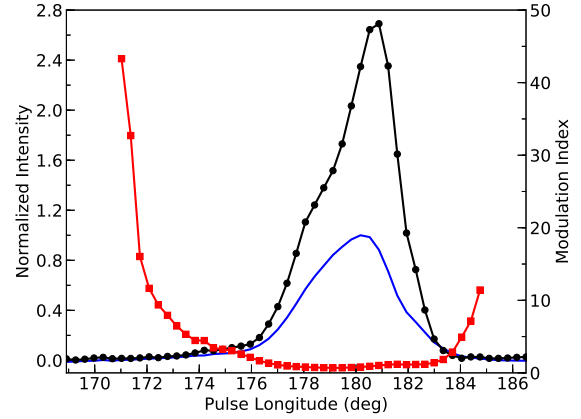


Figure 3. The integrated pulse profile, the longitude-resolved standard deviation and the longitude-resolved modulation index are displayed in blue, black and red solid lines, respectively.

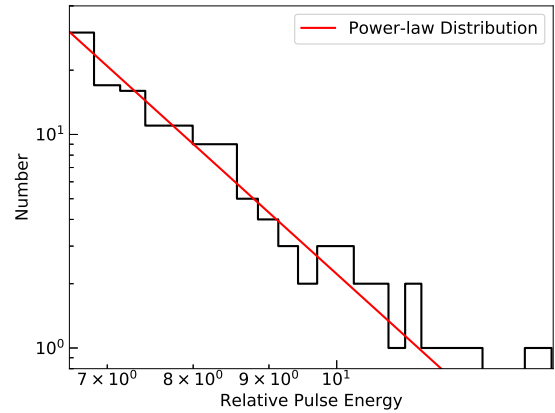


Figure 4. Relative pulse energy distribution for the leading edge of the profile. To obtain a more accurate estimate, only the pulses where the bursts were present are included in the distribution. The best-fitted power-law distribution with estimated index of -6.3 ± 0.3 is shown in the red line.

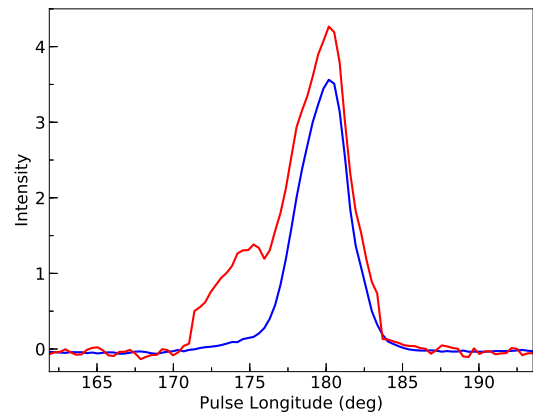


Figure 5. The average pulse profiles in the presence (red) and absence (blue) of the sporadic leading part.

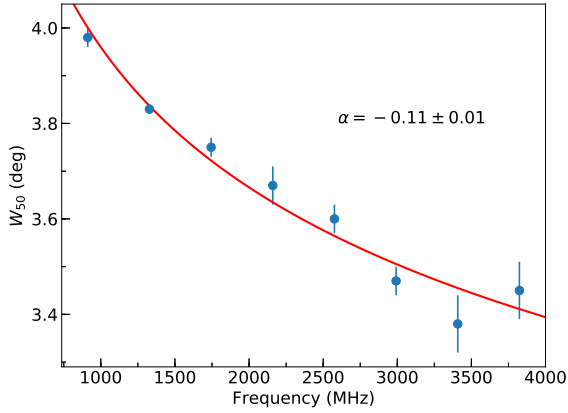


Figure 6. Evolution of the profile width with the observing frequency. The red curve represents the best power-law fit with an index estimated to be $\alpha = -0.11 \pm 0.01$.

since the leading part emission is below the 50 per cent level of the peak. The best power-law fit gives an index of $\alpha = -0.05 \pm 0.01$. The pulse width measurements are available over a broad range of radio frequencies. The relation between pulse width and frequency for 150 normal pulsars has been studied by [Chen & Wang \(2014\)](#). Clear pulse width narrowing with increasing frequency for about 54% of their pulsars were reported. The best-fit Thorsett indices are distributed within -1 and 0 , and peaked near 0 . [Posselt et al. \(2021\)](#) presented measurements of a homogeneous large sample of pulse widths from the Thousand-Pulsar-Array programme on the MeerKAT telescope. The pulse width as a function of the rotation period is described with a steep power-law. The power-law index is estimated to be -0.63 ± 0.06 using orthogonal distance regression technique. In addition, a monotonic behaviour with frequency is shown in the measured width changes. The core and conal component widths versus period in normal pulsars were measured to have a lower boundary line that closely follows the power-law relation with index of -0.5 ([Skrzypczak et al. 2018](#)). [Xu et al. \(2021\)](#) systematically investigated the frequency evolution behaviour of profile widths for 74 pulsars. The power-law indices of most pulsars are measured to be around -0.15 . The profile evolution with observing frequency is consistent with the RFM effect, where the high-frequency emission is assumed to be generated at a lower altitude and vice versa ([Cordes 1978](#)). The magnetospheric electron density is expected to decrease with increasing altitude, predicting that the radio beam expands with decreasing frequency ([Ruderman & Sutherland 1975](#)).

Measuring the altitudes of radiation locations is of great importance for the research of pulsar radiation mechanism as well as research for physical processes in pulsar magnetospheres. The emission altitudes can be estimated by considering the geometrical properties of the radiation beam, which is proposed by [Cordes \(1978\)](#) and developed further by [Kijak & Gil \(1997\)](#). The inclination angle and impact angle are basic parameters for measuring the altitude. They can be obtained by fitting the linear polarization position angle curve in the rotating vector model ([Radhakrishnan & Cooke 1969](#)). Furthermore, the polarization behaviour serves the purpose of revealing whether the leading part can be classified as a conal component or merely an extension of the core component. However, the emission geometry cannot be determined for PSR J1401–6357 due to the lack of calibrated observations for polarization.

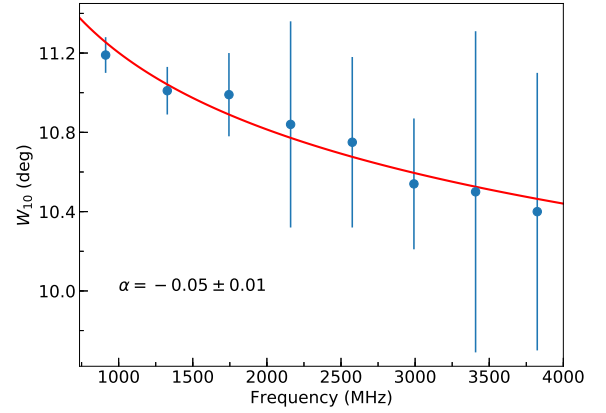


Figure 7. Frequency evolution of the profile width during the leading burst state. The red curve represents the best power-law fit with an index estimated to be $\alpha = -0.05 \pm 0.01$.

3.2 Pulse nulling

As shown in Figure 1, the pulsed emission switches simultaneously from burst state to null state (and vice versa) across the different frequencies. This behaviour is broadly confirmed by a visual inspection of the entire data, which implies that pulse nulling in this pulsar appears to be broadband.

The investigation of pulse energy distribution provides insights into the radio pulsar emission mechanism and the physical state of pulsar magnetospheres. PSR J1401–6357 was reported to exhibit atypically broad pulse energy distribution at 1352 MHz ([Burke-Spolaor et al. 2012](#)). Figure 8 presents the energy distributions for the on-pulse and off-pulse windows after averaged over the whole frequency band, which are calculated using the standard method described by [Ritchings \(1976\)](#). The on-pulse window, ranging from 170° to 190° , is determined by inspection of the integrated pulse profile. The off-pulse window is determined in the off-pulse region with the size equal to the on-pulse window. The normalized on-pulse and off-pulse energies are calculated for each pulsar rotation by integrating the energies in the on-pulse and off-pulse windows, respectively, and then divided by the mean on-pulse energy obtained from all integrations. The off-pulse energy represents the Gaussian random noise contributed by the system temperature, which can be well modeled with a Gaussian distribution centered around zero. The distribution width corresponds to the rms fluctuations of the data. It is noted that the null and burst pulse distributions are indistinguishable in the on-pulse energy distribution due to the low S/N burst pulses mixing with the null pulse distribution and a small number of null pulses. The statistical estimation on the NF is not applicable. [Burke-Spolaor et al. \(2012\)](#) found that the normal pulsar population is seen to exhibit mostly lognormal pulse energy distributions. It appears that PSR J1401–6357 follows the same trend. The Kolmogorov-Smirnov (KS) hypothesis test is applied to check whether or not the observed distribution can be described by a lognormal distribution. The obtained p -value of the lognormality hypothesis test is greater than the threshold value of 0.05 , which indicates that the observed distribution is consistent with a lognormal distribution. The lognormal statistics are intrinsic to pulsar emission, which can be interpreted in terms of a pure stochastic growth theory (SGT) ([Cairns et al. 2003](#)). The associated pulsar emission mechanism is suggested to involve with only linear processes.

To improve the detection sensitivity for the single pulses for nulling

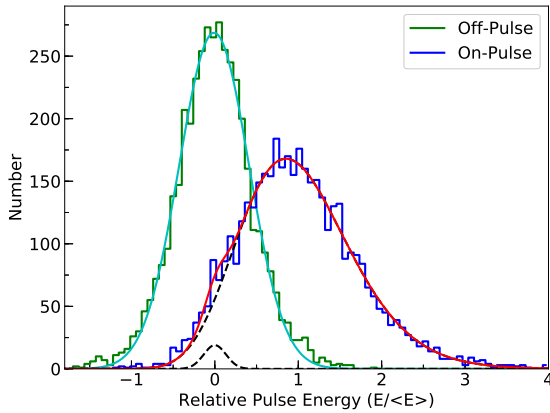


Figure 8. Pulse energy histograms for the on-pulse (blue) and off-pulse (green) windows. The energies are normalized by the mean on-pulse energy. The cyan line represents the off-pulse noise model fit. The red line indicates the distribution expected from a combination of a Gaussian and a lognormal distributions (black dashed lines).

analysis, the signals from the different subbands are combined. We follow the procedure presented by [Bhattacharyya et al. \(2010\)](#) for identification of individual nulls, in which pulses with intensity smaller than $3\sigma_{ep}$ are classified as nulls, where σ_{ep} is the uncertainty in the pulse energy calculated from the root-mean-square energy in the off-pulse window. To further identify the null pulses with more accuracy, a visual inspection is carried out on the pulse sequence and the mislabeled nulls and bursts are redressed. There are 95 null pulses identified and the NF is estimated to be $2.26 \pm 0.23\%$. The uncertainty of NF is simply given by $\sqrt{n_p/N}$, where n_p is the number of null pulses and N is the total number of observed pulses. Our determined NF is larger than that estimated by [Wang et al. \(2007\)](#) at 1369 MHz. A total of 13 blocks of burst state are identified from the whole set of observations. The histograms for null length and burst length are formed and displayed in Figure 9. The length distribution of contiguous nulls is apparently dominated by 1-period nulls. The short nulls are predominantly weak normal pulses, which occur randomly among the emission bursts. There are three long null states with durations of 13, 28 and 37 pulses. The durations of burst states vary from 1 pulse to 1514 pulses. The occasional individual strong pulses are found within the null intervals. Figure 10 shows the normalized pulse profiles obtained by integrating pulses in short (blue) and long (red) bursting states. The profile of short duration bursts is wider than that of long duration bursts. In comparison with the profile for the long burst state, the profile for short duration bursts shifts to later longitude by almost 0.7° .

3.3 Subpulse drifting

In general, drifting subpulses, nulling, and mode changing can be detected through visual inspection of the single pulse sequence for bright pulsars. [Backer \(1973\)](#) and [Backer et al. \(1975\)](#) developed a systematic approach to measure the drifting features, including the fluctuation spectral studies. This often-used technique is suitable for detecting subpulse drifting in weak pulsars. The drifting is characterized by two periodicities: P_2 (the longitudinal separation between two adjacent drift bands) and P_3 (the interval over which the subpulses repeat at a specific location within the pulse window). To detect a regular intensity variation, the longitude-resolved fluctua-

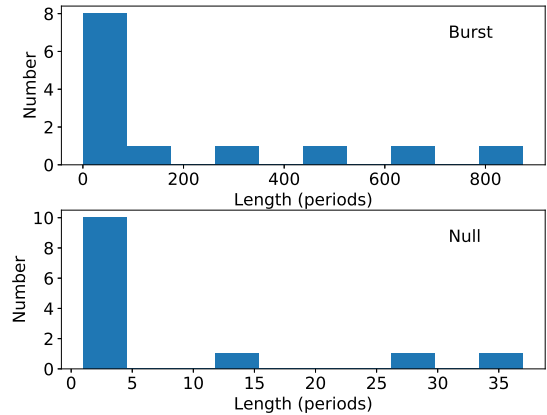


Figure 9. Histograms of observed null length and burst length for PSR J1401–6357.

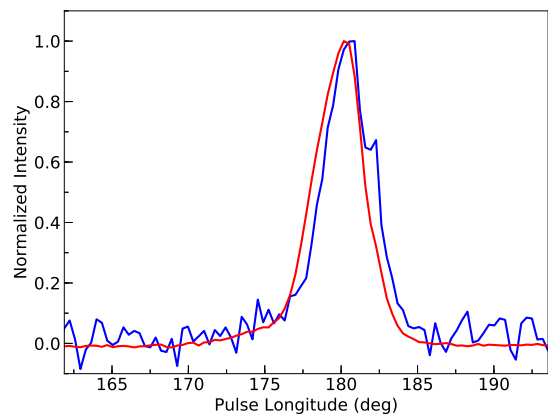


Figure 10. The average pulse profile by integrating pulses in short duration bursting states within the null intervals is shown in blue. The average pulse profile by integrating pulses in the long burst states is shown in red.

tion spectrum (LRFS) is calculated to estimate P_3 ([Backer 1970a](#)). To do that, the pulse-stack is divided into blocks of 512 successive pulses, and then the discrete Fourier transform (DFT) is performed along each longitude bin within the pulse window on these blocks. The final spectrum is obtained by averaging the fluctuation power across all longitudes along the pulse window. An example is presented in Figure 11, which is used to determine the time evolution of periodic modulation at 912 MHz. The drift tracks with regions of enhanced intensity are visible, which indicate the changes in periodic modulation with time. The lower panel shows the averaged power spectrum across all blocks, which also demonstrates the presence of a high-frequency modulation feature ranging from 0.4 to 0.5 cycle period⁻¹. The time variation of the modulation power is shown in the left panel, where the periodic modulation vanishes between pulse numbers 1500 and 2750. The temporal subpulse drifting behaviour across multiple frequencies is investigated in order to reveal the simultaneity in the changes of the subpulse drifting across the different frequencies, which will also reveal the broadband nature of the subpulse drifting in this pulsar.

To describe drifting in an averaged sense, the LRFS averaged over the whole observing frequency band is shown in the main panel of Figure 12. A distinct region of power excess is identi-

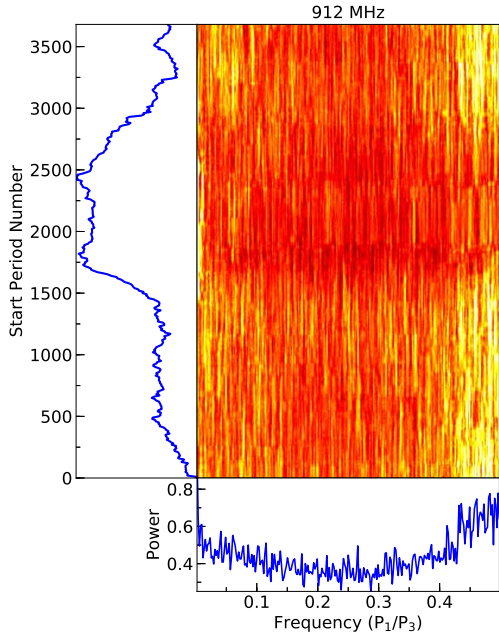


Figure 11. Main: The time-varying longitude-resolved fluctuation spectra. Bottom: The averaged spectrum across all times showing the presence of high-frequency modulation feature. Left: The time variation of the modulation power.

fied in the corresponding pulse longitude from 178° to 182° . The high-frequency structured subpulse modulation feature appears to range from 0.4 to 0.5 cycle period $^{-1}$ (P_1/P_3) at the eight observing frequencies. The pulsar is classified as a diffuse drifter, because the broad modulation feature is not separated from the alias border clearly (Weltevrede et al. 2006).

To determine whether the subpulses are amplitude-modulated drifting or phase-modulated drifting, the two-dimensional fluctuation spectrum (2DFS) is calculated by performing two-dimensional DFT along the vertical lines and the lines with various slopes (Edwards & Stappers 2002). Following the same procedures for calculating the LRFS, the pulse-stack is divided in blocks of 512 successive pulses and the spectra of the different blocks are then averaged to obtain the final spectra. In Figure 13, the 2DFS averaged over the whole observing frequency band is shown in the main panel. The left panel shows the horizontally integrated power. The main feature at the same horizontal position as in the LRFS is presented, corresponding to the same P_3 value. To determine the value of P_3 , a similar method described by Weltevrede et al. (2006) is adopted, which involves calculating the centroid of a rectangular region in the 2DFS containing the feature. The uncertainty is estimated from the power in a region, which contains only noise, in the 2DFS. The corresponding drifting periodicity is estimated to be $P_3 = 2.3 \pm 0.3P_1$ at the eight frequencies. The pattern repetition frequency along the pulse longitude is denoted in the horizontal axis of the 2DFS, which is expressed as P_1/P_2 . It is noted that a clear double-peaked feature in 2DFS is present, which indicates that the apparent drift sense changes during the observation. The values of P_2 are estimated to be -7 ± 3 and 8 ± 3 degrees, which exceed the pulse width. This means that only one subpulse is visible in a single pulse, and the drifting

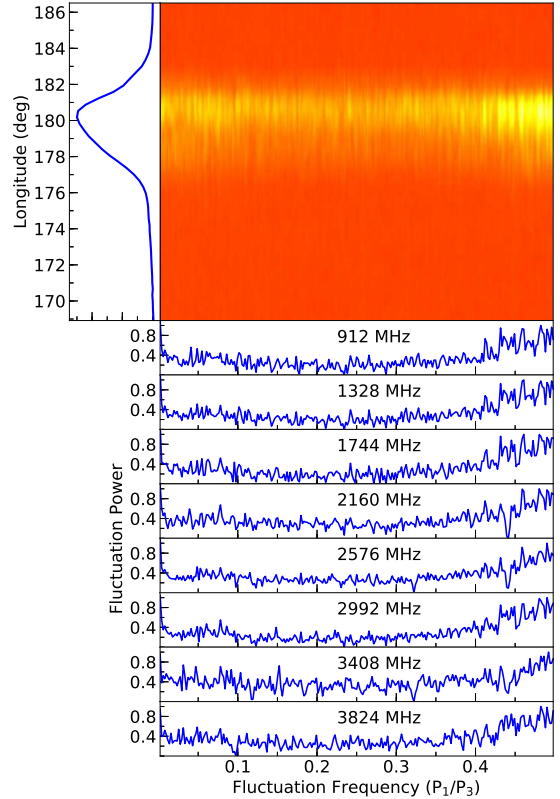


Figure 12. Main: The longitude-resolved fluctuation power spectra averaged over the whole observing frequency band. The abscissa is the frequency of the drifting periodicity and the ordinate is the profile longitude. The intensity of the drifting periodicities as a function of pulse longitude is plotted in color contours. The total power profile is shown in the left panel. The integral power spectra at the eight frequencies are presented in the lower panel.

appears as an amplitude modulation rather than as a phase modulation (Asgekar & Deshpande 2005). The drift bands often appear very nonlinear, and therefore the magnitude of P_2 probably possesses little meaning. Alternatively, the subpulse phase jump or swing could produce the double peaked feature (Edwards et al. 2003). The fluctuation spectra at the eight different frequencies are the same, which imply that the subpulse drifting is independent of the observing frequency.

In order to rule out the possibility that the occasional occurrence of strong subpulses and RFI are dominating the spectra and therefore lead to misleading conclusions, a similar method is adopted to further demonstrate the authenticity of the periodic fluctuations (Weltevrede et al. 2006). This involves randomizing the order of the pulse sequence, and then the LRFSs and 2DFSs are calculated from the newly formed pulse stack. No well-defined P_3 in this process is detected in the emission window and the noise window, which confirms the significance of the drift features.

Recently, the quasi-periodic fluctuation features are broadly categorized into two groups: longitude-modulated drifting and periodic amplitude modulation (Basu et al. 2019a). Subpulse drifting is shown to be profile dependent, with the phenomenon found in the conal components and absent in the central core emission (Basu et al. 2019a). The amplitude-modulated drifting is thought to be a different phenomenon from subpulse drifting (Basu et al. 2016, 2017). A survey

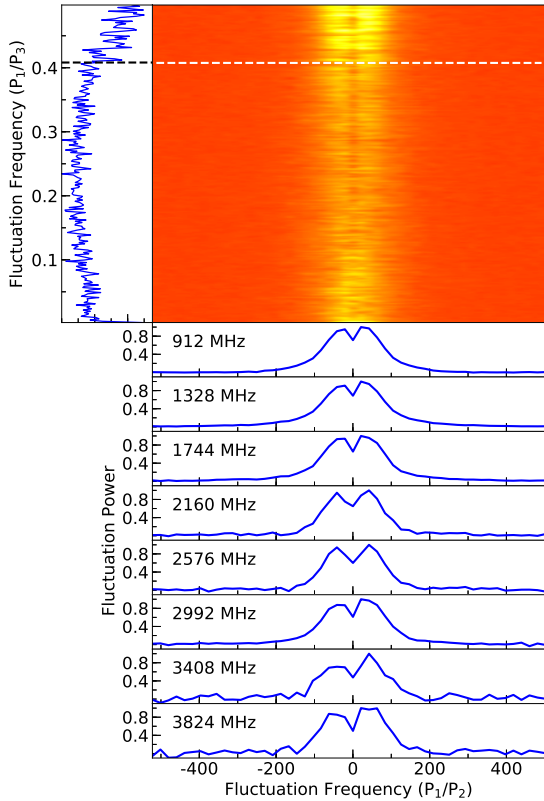


Figure 13. Main: Two-dimensional fluctuation power spectra averaged over the whole observing frequency band. The units of the horizontal axis are P_1/P_2 , where P_2 is the horizontal separation between drift bands in time units. The power in the 2DFS is horizontally integrated, producing the left power spectra. The vertically integrated power spectra at the eight frequencies are presented in the lower panel.

of the periodic amplitude modulation and periodic nulling has been carried out in the pulsar population by [Basu et al. \(2020c\)](#). These longitude-stationary behaviours appear to occur across the entire profile in both the core and conal components simultaneously. The core component in some pulsars is suggested to exhibit long periodic fluctuation structure, which is not classified as subpulse drifting ([Rankin 1986](#)). Pulsars with core-single profiles are found to exhibit diffuse fluctuation features with no discernible longitude shift ([Basu et al. 2016](#)). Highly periodic longitude-stationary amplitude modulation is revealed to be temporal-dependent in the core-single radio pulsar B1946+35 ([Mitra & Rankin 2017](#)). The longitude-stationary non-drift amplitude modulation in PSR J1048–5832 is argued to be associated with periodic mode changing ([Yan et al. 2020](#)). The pulsars B2000+40, J2048–1616 and J2006–0807 with core-cone profiles show the presence of periodicity in association with nulling as well as subpulse drifting ([Basu et al. 2020b](#); [Wang et al. 2021](#); [Basu et al. 2019b](#)). The fluctuation spectral analysis reveals that the shorter modulation periodicities are associated with the subpulse drifting and absent in the central core component. The longer periodicities are associated with the periodic nulling behaviour. Therefore, the detected periodic behaviour in the core-single pulsar J1401–6357 can be interpreted as longitude-stationary amplitude modulation.

4 DISCUSSION

In general, the observed drifting periodicity can either be the true drifting periodicity for complete Nyquist sampling or an aliased drift periodicity for incomplete Nyquist sampling. In a sparking gap model, the spark-associated plasma columns drift due to an $E \times B$ drift, which depends on both the pulse period and its derivative ([Ruderman & Sutherland 1975](#)). In the presence of aliasing, it is impossible to determine the physical conditions of the pulsar from the apparent drift rate. The lower value of P_3 can result from aliasing of a higher $E \times B$ drift, and vice versa. As shown in Figure 13, the feature in the 2DFS is not clearly separated from the alias border, and the power in that feature could come from drift bands of different alias modes. It is a challenge to relate the measured drifting periodicity to the true drift rate of the emission sparks. A visual inspection is carried out on the pulse sequence, which reveals that the apparent drift direction is constantly changing during the observation. [Weltevrede et al. \(2006\)](#) simulated a pulse sequence with drifting that constantly crosses the $P_3 = 2P_1$ alias border to illustrate this effect. There are a number of pulsars that show evidence for drift reversals. For example, PSR B2303+30 shows a clear double peaked feature in its 2DFS ([Redman et al. 2005](#)). The feature follows a steady even-odd pattern in the intense mode B emission, which is explained by the constantly changing drift patterns in terms of varying subbeam rotation rates. PSR B0826–34 is reported to show drift reversals, and it continuously changes the apparent drift direction via longitude stationary subpulse modulation ([Gupta et al. 2004](#); [Esamdin et al. 2005](#)). Furthermore, there is no evidence for the existence of a pulsar sub-population with subpulse drifting that locates close to the $P_3 = 2P_1$ Nyquist limit ([Wright 2003](#)).

We find that pulse nulling and subpulse drifting phenomena in PSR J1401–6357 are consistent across the ultrawide frequency band. The occurrence of pulse nulling appears highly concurrent across the different frequency bands, which is consistent with the behaviour reported by [Gajjar et al. \(2014\)](#). A systematic and simultaneous multi-frequency study of pulsars shows that subpulse drifting and pulse nulling are broadband in nature ([Naidu et al. 2017](#)). The switching between multiple drift rates with distinct P_3 occurs simultaneously across all the observed frequencies. The broadband emission related to the localized emission processes is proposed to occur close to the pair production fronts near the polar caps ([Melrose 1996](#)). Intrinsic models invoking extinction of the sparking region are proposed, in which the entire magnetosphere is undergoing rapid changes causing cessation of the radio emission. There is increasing evidence that the cessation of emission is associated with the disruption of the entire particle flow. The switching between the radio-quiet ‘off’ and radio-loud ‘on’ states in the intermittent pulsar B1931+24 was found to be correlated with the slowing down rate of the pulsar ([Kramer et al. 2006](#)). [Lyne et al. \(2010\)](#) presented the correlated changes between the shape of the pulse profile and the timing noise for six pulsars. Furthermore, the implied broadband nature of pulse nulling and subpulse drifting also suggests that the geometry of pulsar emission, including variations in the emission height, is unlikely to affect the behaviour of the two phenomena. The nulling and drifting are probably governed by the gap potential and magnetic field in the polar gap, although counterexamples are reported in multifrequency observations. Different P_3 values at 21 cm and 92 cm for PSRs J1822–2256, J1901–0906, B1844–04, B2016+28, and B2045–16 are suggested ([Weltevrede et al. 2006, 2007](#)). The frequency dependence of a well known drifter PSR B0031–07 was investigated by [Smits et al. \(2005\)](#). In the context of the carousel model, several ideas have been advanced to explain this frequency-dependent behaviour of subpulses.

Davies et al. (1984) suggested that the magnetic field is not purely dipolar, but it includes a multipole component with contra-rotation twisting at large radii. Edwards & Stappers (2003) proposed the finite size and shape of beamlets resulting in their cross sections being slightly shifted relative to the line of sight as the frequency-dependent beamlets move in magnetic colatitude. Recently, McSweeney et al. (2019) developed an idea to obtain quantitative predictions of how subpulses shift with frequency by speculating that aberration and retardation effects are the dominant cause.

5 CONCLUSIONS

Using the highly sensitive ultrawideband Parkes observations, we have performed detailed single pulse analysis for PSR J1401–6357. From the fluctuation spectral analysis, this pulsar is identified as a diffuse subpulse drifter for the first time. The subpulse modulation is extended toward the $P_3 = 2P_1$ alias border, and the 2DFS shows a feature that is split by the vertical axis owing to the two apparent drift directions in the pulse sequence. Our results confirm and further strengthen the conclusions that pulse nulling and subpulse drifting are broadband phenomena. One hour single pulse observations are sufficient for the identification of these phenomena themselves. Our ultrawideband observations of the individual pulses from PSR J1401–6357 contribute to the generalization of the broadband behaviour of pulse nulling and subpulse drifting.

ACKNOWLEDGEMENTS

We would like to thank the anonymous referee for providing constructive suggestions, which helped in improving the paper. This work is partially supported by the National Key Research and Development Program of China (No. 2022YFC2205203), the National Natural Science Foundation of China (NSFC grant No. 11988101, U1838109, 12041304, 12041301, 11873080, U1631106), the National SKA Program of China (2020SKA0120100), the Chinese Academy of Sciences Foundation of the young scholars of western (No. 2020-XBQNXZ-019), and Xinjiang Key Laboratory of Radio Astrophysics (No. 2022D04058). Z.G.W. is supported by the 2021 project Xinjiang uygur autonomous region of China for Tianshan elites. J.L.C. is supported by the Natural Science Foundation of Shanxi Province (20210302123083), and the Scientific and Technological Innovation Programs of Higher Education Institutions in Shanxi (grant No. 2021L470). H.W. is supported by the Scientific and Technological Innovation Programs of Higher Education Institutions in Shanxi (Grant No. 2021L480). W.M.Y. is supported by the CAS Jianzhijia project. H.G.W. is supported by the 2018 project of Xinjiang uygur autonomous region of China for flexibly fetching in upscale talents. S.R.C. is supported by the student innovation project of Yuncheng university (20220940). The Parkes radio telescope, ‘Murriyang’, is part of the Australia Telescope National Facility which is funded by the Australian Government for operation as a National Facility managed by CSIRO.

DATA AVAILABILITY

The data underlying this article are available in the Parkes Pulsar Data Archive at <https://data.csiro.au>, and can be accessed with the source name J1401–6357.

REFERENCES

- Asgekar A., Deshpande A. A., 2005, *MNRAS*, **357**, 1105
 Backer D. C., 1970a, *Nature*, **227**, 692
 Backer D. C., 1970b, *Nature*, **228**, 42
 Backer D. C., 1973, *ApJ*, **182**, 245
 Backer D. C., Rankin J. M., Campbell D. B., 1975, *ApJ*, **197**, 481
 Basu R., Mitra D., Melikidze G. I., Maciesiak K., Skrzypczak A., Szary A., 2016, *ApJ*, **833**, 29
 Basu R., Mitra D., Melikidze G. I., 2017, *ApJ*, **846**, 109
 Basu R., Mitra D., Melikidze G. I., Skrzypczak A., 2019a, *MNRAS*, **482**, 3757
 Basu R., Paul A., Mitra D., 2019b, *MNRAS*, **486**, 5216
 Basu R., Mitra D., Melikidze G. I., 2020a, *MNRAS*, **496**, 465
 Basu R., Lewandowski W., Kijak J., 2020b, *MNRAS*, **499**, 906
 Basu R., Mitra D., Melikidze G. I., 2020c, *ApJ*, **889**, 133
 Basu R., Melikidze G. I., Mitra D., 2022, *ApJ*, **936**, 35
 Bhattacharyya B., Gupta Y., Gil J., 2010, *MNRAS*, **408**, 407
 Brinkman C., Mitra D., Rankin J., 2019, *MNRAS*, **484**, 2725
 Burke-Spolaor S., et al., 2012, *MNRAS*, **423**, 1351
 Cairns I. H., Johnston S., Das P., 2003, *MNRAS*, **343**, 512
 Chen J. L., Wang H. G., 2014, *ApJS*, **215**, 11
 Cordes J. M., 1978, *ApJ*, **222**, 1006
 Cordes J. M., Shannon R. M., 2008, *ApJ*, **682**, 1152
 Davies J. G., Lyne A. G., Smith F. G., Izvekova V. A., Kuzmin A. D., Shitov I. P., 1984, *MNRAS*, **211**, 57
 Deng Z.-L., Gao Z.-F., Li X.-D., Shao Y., 2020, *ApJ*, **892**, 4
 Deng Z.-L., Li X.-D., Gao Z.-F., Shao Y., 2021, *ApJ*, **909**, 174
 Drake F. D., Craft H. D., 1968, *Nature*, **220**, 231
 Edwards R. T., Stappers B. W., 2002, *A&A*, **393**, 733
 Edwards R. T., Stappers B. W., 2003, *A&A*, **407**, 273
 Edwards R. T., Stappers B. W., van Leeuwen A. G. J., 2003, *A&A*, **402**, 321
 Esamdin A., Lyne A. G., Graham-Smith F., Kramer M., Manchester R. N., Wu X., 2005, *MNRAS*, **356**, 59
 Gajjar V., Joshi B. C., Wright G., 2014, *MNRAS*, **439**, 221
 Gao Z. F., Shan H., Wang H., 2021, *Astronomische Nachrichten*, **342**, 369
 Geppert U., Rheinhardt M., Gil J., 2003, *A&A*, **412**, L33
 Geppert U., Basu R., Mitra D., Melikidze G. I., Szkudlarek M., 2021, *MNRAS*, **504**, 5741
 Gupta Y., Gil J., Kijak J., Sendyk M., 2004, *A&A*, **426**, 229
 Herfindal J. L., Rankin J. M., 2007, *MNRAS*, **380**, 430
 Hobbs G., et al., 2004, *MNRAS*, **352**, 1439
 Hobbs G., et al., 2011, *Publ. Astron. Soc. Australia*, **28**, 202
 Hobbs G., et al., 2020, *Publ. Astron. Soc. Australia*, **37**, e012
 Hotan A. W., van Straten W., Manchester R. N., 2004, *Publ. Astron. Soc. Australia*, **21**, 302
 Johnston S., Kerr M., 2018, *MNRAS*, **474**, 4629
 Jones D. I., 2012, *MNRAS*, **420**, 2325
 Kijak J., Gil J., 1997, *MNRAS*, **288**, 631
 Kramer M., 1994, *A&AS*, **107**, 527
 Kramer M., Lyne A. G., O’Brien J. T., Jordan C. A., Lorimer D. R., 2006, *Science*, **312**, 549
 Lyne A., Hobbs G., Kramer M., Stairs I., Stappers B., 2010, *Science*, **329**, 408
 Manchester R. N., Hobbs G. B., Teoh A., Hobbs M., 2005, *AJ*, **129**, 1993
 McSweeney S. J., Bhat N. D. R., Wright G., Tremblay S. E., Kudale S., 2019, *ApJ*, **883**, 28
 Melrose D. B., 1996, in Johnston S., Walker M. A., Bailes M., eds, *Astronomical Society of the Pacific Conference Series Vol. 105*, IAU Colloq. 160: Pulsars: Problems and Progress. p. 139
 Mitra D., Rankin J., 2017, *MNRAS*, **468**, 4601
 Mitra D., Rankin J., Arjunwadkar M., 2016, *MNRAS*, **460**, 3063
 Naidu A., Joshi B. C., Manoharan P. K., KrishnaKumar M. A., 2017, *A&A*, **604**, A45
 Posselt B., et al., 2021, *MNRAS*, **508**, 4249
 Qiao G., Manchester R. N., Lyne A. G., Gould D. M., 1995, *MNRAS*, **274**, 572
 Radhakrishnan V., Cooke D. J., 1969, *Astrophys. Lett.*, **3**, 225
 Rankin J. M., 1983, *ApJ*, **274**, 333
 Rankin J. M., 1986, *ApJ*, **301**, 901

- Rankin J., 2022, *MNRAS*, 514, 3202
- Redman S. L., Wright G. A. E., Rankin J. M., 2005, *MNRAS*, 357, 859
- Ritchings R. T., 1976, *MNRAS*, 176, 249
- Rosen R., McLaughlin M. A., Thompson S. E., 2011, *ApJ*, 728, L19
- Ruderman M. A., Sutherland P. G., 1975, *ApJ*, 196, 51
- Sieber W., Reinecke R., Wielebinski R., 1975, *A&A*, 38, 169
- Skrzypczak A., Basu R., Mitra D., Melikidze G. I., Maciesiak K., Koralewska O., Filothodoros A., 2018, *ApJ*, 854, 162
- Smits J. M., Mitra D., Kuijpers J., 2005, *A&A*, 440, 683
- Szary A., van Leeuwen J., 2017, *ApJ*, 845, 95
- Timokhin A. N., 2010, *MNRAS*, 408, L41
- Wang N., Manchester R. N., Johnston S., 2007, *MNRAS*, 377, 1383
- Wang Z., et al., 2021, *ApJ*, 923, 259
- Weltevrede P., Edwards R. T., Stappers B. W., 2006, *A&A*, 445, 243
- Weltevrede P., Stappers B. W., Edwards R. T., 2007, *A&A*, 469, 607
- Wright G. A. E., 2003, *MNRAS*, 344, 1041
- Wright G., 2022, *MNRAS*, 514, 4046
- Wright G., Weltevrede P., 2017, *MNRAS*, 464, 2597
- Xu X., et al., 2021, *ApJ*, 917, 108
- Yan W. M., Manchester R. N., Wang N., Wen Z. G., Yuan J. P., Lee K. J., Chen J. L., 2020, *MNRAS*, 491, 4634
- Yan F.-Z., Gao Z.-F., Yang W.-S., Dong A.-J., 2021, *Astronomische Nachrichten*, 342, 249
- Zhang B., Qiao G. J., Lin W. P., Han J. L., 1997, *ApJ*, 478, 313
- van Leeuwen J., Timokhin A. N., 2012, *ApJ*, 752, 155

This paper has been typeset from a $\text{\TeX}/\text{\LaTeX}$ file prepared by the author.